www.nature.com/scientificreports

scientific reports

OPEN

Consolidation behaviour of AZ80 magnesium chips: influence of compaction pressure and holding time on porosity, interfaces and mechanical response

A. Murillo-Marrodán[1]✉, **E. García**[1] & **T. Nakata**[2]

Solid-state recycling of magnesium alloys relies on effective pre-compaction to convert loose machining chips into dense precursors suitable for downstream processing. This study investigates the consolidation mechanisms of AZ80 Mg chips containing residual water-based lubricants, compacted in a single-action hydraulic press without prior cleaning. The compaction pressure, holding time, and pressure evolution were analyzed to determine their influence on briquette quality. The findings demonstrated that holding time, rather than peak pressure, was the governing factor for densification. Extended holding promoted internal stress redistribution and geometric adaptation, facilitating pore collapse and yielding green densities of ~ 91–92% with uniform axial distribution, while short holding times limited effective stress transmission, resulting in heterogeneous density gradients. Microstructural analysis revealed that while native oxide barriers persisted, preventing full metallurgical bonding, extended holding achieved sub-micron interfacial spacing and effective geometric closure. Hardness mapping indicated that shorter holding times retained higher hardness values (~ 110–116 HV), consistent with high localized work hardening and incomplete stress redistribution. In addition, compression tests revealed that stiffness was governed by interfacial integrity rather than bulk density. Therefore, samples with superior geometric sealing exhibited significantly higher stiffness (2964 MPa) compared to denser samples with poorer interfacial locking. These results indicate that optimizing interfacial contact through load maintenance is critical for producing stable briquettes, providing a pathway for robust solid-state recycling of AZ80 alloys.

Keywords AZ80 Mg alloy, Machining chips, Solid-state recycling, Cold compaction, Residual lubricants

The transition toward sustainable manufacturing demands efficient recycling strategies to minimize resource and energy consumption. Mg alloys are particularly attractive candidates, offering low density and high specific strength suitable for lightweight automotive and aerospace applications[1,2]. However, component manufacturing still requires substantial machining, with even high-yield processes such as die casting generating around 7% scrap, and forged parts exhibiting even higher losses[3]. In aerospace applications, buy-to-fly ratios can reach 15–20, indicating substantial material loss during machining[4]. Given these material losses, the high energy demand of primary Mg production further raises sustainability and cost concerns[5], reinforcing the need for effective recycling routes for Mg scrap.

Conventional recycling of lightweight alloy chips through remelting involves considerable energy consumption and oxidation, often leading to microstructural degradation due to oxide inclusions and loss of alloying elements[6,7]. This issue is particularly critical for machining chips, which are typically contaminated with cutting fluids and exhibit high surface area, making them highly reactive to humidity[8]. In addition, they often display a lamellar surface morphology indicative of adiabatic shear banding[9], which increases their susceptibility to oxidation. In AZ31B recycling, persistent MgO inclusions remained despite refinement, limiting

[1]Department of Mechanics, Design and Industrial Management, University of Deusto, Avda Universidades 24, 48007 Bilbao, Spain. [2]Research Center for Advanced Magnesium Technology, Nagaoka University of Technology, Nagaoka 940-2188, Japan. ✉email: alberto.murillo@deusto.es

chip additions to ~ 10%. Higher fractions caused grain coarsening and mechanical degradation, highlighting the intrinsic limitations of remelting contaminated scrap[10].

In response, solid-state recycling (SSR) has emerged as a promising route to convert metallic chips into fully dense products without melting, using plastic deformation instead, thereby preserving alloy chemistry and substantially lowering environmental impact[11]. Among the SSR routes, those based on bulk deformation of Mg generally require a pre-compaction stage to consolidate loose chips into preforms. In particular, severe plastic deformation (SPD) methods such as high-pressure torsion (HPT)[12], extrusion-shear (ES)[13] or equal-channel angular pressing (ECAP)[14,15] rely on cold pressing (in some cases hot sintering)[16] to produce disks or billets capable of sustaining the intense shear strains imposed during deformation. Likewise, conventional hot extrusion–based SSR routes may employ cold[17,18] or hot[19] pre-compaction, or sintering[20], to obtain briquettes with sufficient mechanical integrity.

The efficiency of SSR routes can be affected by the quality of the pre-compacted precursor. During pre-compaction, plastic deformation promotes intimate chip–chip contact and initiates the fragmentation of thin oxide surface films that hinder metallurgical bonding[11]. According to the film bonding theory[21], this fragmentation of oxide film is generated by surface expansion due to plastic deformation. Thus, it requires shear deformation, which can arise from the random orientation of chips under high applied pressure, leading to localized plastic flow[22] and improved green densification. Consequently, a well-compacted precursor could reduce the strain demanded in the main SSR step (e.g., extrusion or SPD) to achieve full bonding, whereas insufficient pre-compaction leaves persistent discontinuities, interfaces and oxides that require higher deformation and may degrade mechanical performance[23]. This trend is consistent with powder-metallurgy studies on Mg-based materials, where compaction pressure has been shown to directly control green porosity and, consequently, the mechanical behaviour after consolidation[24]. In this line, Ji et al.[25] observed that at low extrusion ratios, where shear strain is insufficient, the recycled alloy loses plasticity, and the presence of large and unbroken MgO particles does not strengthen the material, despite of the beneficial hardening that can arise when oxide fragments are small and well dispersed.

In previous SSR studies of Mg alloys, either chips are generated by dry machining[18], or cleaned prior to pre-compaction using sequences that combine distilled-water rinsing[13], acetone[26,27], ethanol degreasing[16], ultrasonic cleaning[13,16,28] or drying[26]. However, the relevance of this cleaning step has not been assessed, and the effect of residual lubricants on densification and early bonding remains unclear. Wang et al.[29] reported successful consolidation of AZ91D chips without conventional cleaning using a compacting–sintering–extrusion route, showing that surface condition can influence bonding even before severe deformation. Yet, in plastic-deformation-based SSR routes, compaction parameters beyond the maximum applied pressure, or holding time-pressure relation, have rarely been examined despite their potential to promote localized oxide disruption and improve precursor densification.

In this work, AZ80 machining chips containing residual water-based lubricants were compacted without prior cleaning, and the effects of compaction pressure, holding time and pressure evolution during dwell were assessed. The aim is to clarify how controlled pre-compaction influences green density, the partial fragmentation of native oxide films and the mechanical integrity of the resulting briquettes, thereby determining their suitability for subsequent solid-state recycling by plastic deformation.

Materials and methods

AZ80-T5 Mg alloy chips characterization

The material used in this study consists of extruded AZ80 Mg alloy chips in the T5 condition, produced by turning with a water-based emulsion containing 3 vol.% mineral oil. The coolant was delivered at a flow rate of 23.3 L min^{-1} through a directed flood-cooling system with nozzles positioned at 10 mm from the tool edge. The chemical composition of the initial AZ80 alloy was analyzed by an inductively coupled plasma method. The measured compositions are presented in Table 1.

The chip geometry was characterized by measuring the dimensions of several representative samples under optical microscopy. The average chip width was 3.14 ± 0.50 mm and the average length was 5.2 ± 0.7 mm. The chip thickness was 0.20 ± 0.02 mm, and the corresponding area-to-volume ratio (A/V) was approximately 5 mm^{-1}.

The micromorphology and surface condition of the chips were examined by scanning electron microscopy (SEM, JEOL IT-500), by preparing cross-mounted specimens to expose both principal surfaces, as shown in Fig. 1.

The tool–chip contact surface showed a smooth and bright finish with fine, parallel slip marks aligned with the machining direction (Fig. 1b). On this surface, a continuous ultrathin film was visible, though below the resolution needed to distinguish its internal structure. Local areas contained shallow surface pitting and small corrosion marks (Fig. 1c). In comparison, the free surface exhibited a rough, lamellar topography, consisting of stacked and partially separated layers across the chip thickness (Fig. 1d). This surface presented delamination steps, micro-tearing and fine surface cracking, as well as agglomerated oxide particles accumulated along lamellar boundaries and edge features (Fig. 1e). These observations define the as-received surface condition of the chips prior to consolidation.

Element	Mg	Al	Zn	Mn	Si	Fe
Mass fraction/%	Balance	8.2	0.65	0.24	0.03	0.02

Table 1. Chemical composition of AZ80 T5 alloy.

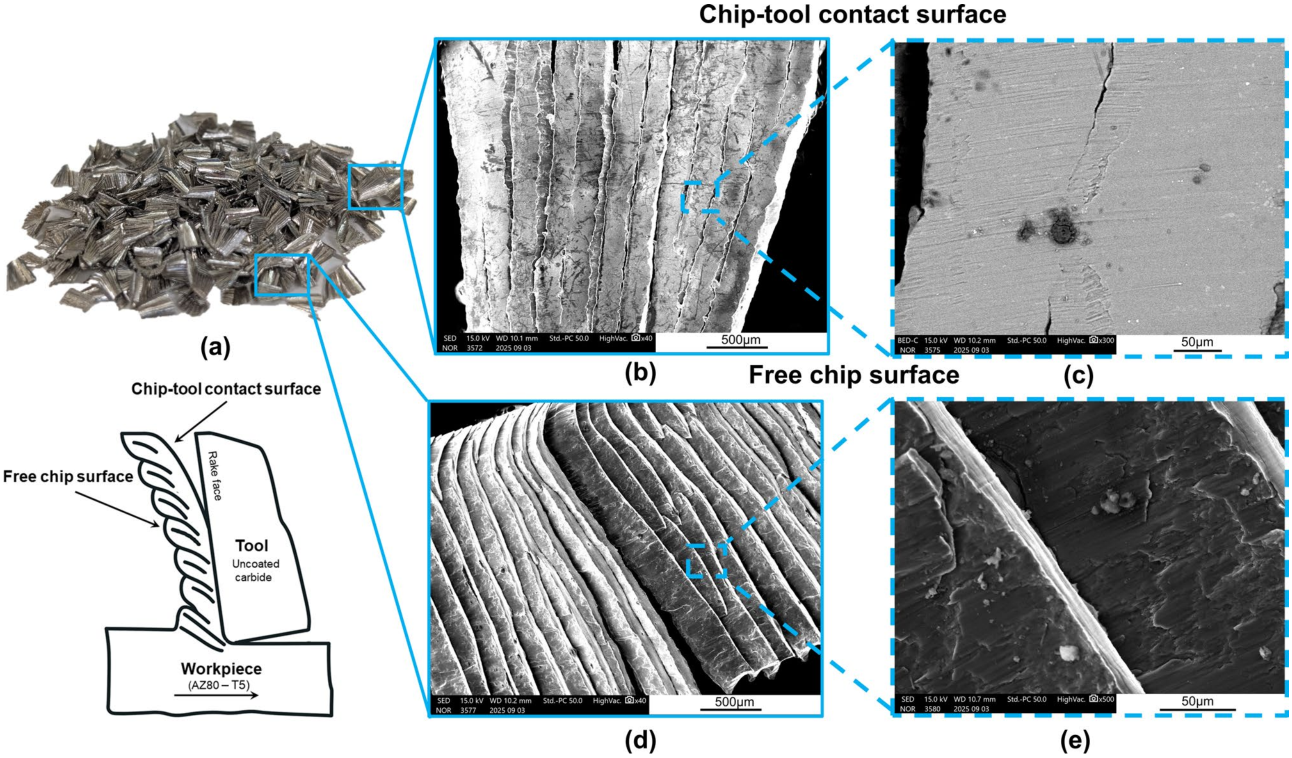

Fig. 1. As-received AZ80 machining chips: (**a**) macroscopic view; chip–tool side showing (**b**) low-magnification SEM image and (**c**) corrosion marks; free surface showing (**d**) lamellar topography and (**e**) agglomerated oxide particles accumulated along lamellar boundaries.

To examine the internal microstructure, chips were mounted in polyester, ground and polished, and lightly etched with Acetic–Picral reagent (picric acid, acetic acid, ethanol and distilled water). This preparation removes the external surface films, so the analysis corresponds to the interior of the chip. Figure 2 illustrates the imaging and analytical approach used to characterize the internal microstructure. SEM observations were conducted in both secondary-electron (SE) and backscattered-electron (BSE) modes, and elemental distributions were assessed using energy-dispersive x-ray spectroscopy (EDS).

BSE imaging (Fig. 2a) enabled distinguishing the α-Mg matrix from the β-$Mg_{17}Al_{12}$ phase through compositional contrast, which is confirmed by the XRD diffractogram shown in Fig. 3. In Fig. 2a, the β phase appeared as angular or elongated particles arranged along bands within the chip interior. SE imaging (Fig. 2b) highlighted surface relief features associated with the internal morphology created during chip formation. EDS mapping confirmed the Mg–Al partitioning between the α matrix and the β phase. A small number of Mn-rich intermetallic particles were also detected, although they were sparse and showed no preferential spatial arrangement. The oxygen signal was strictly confined to the outer edge, confirming surface-limited oxidation with no internal oxide penetration.

The microhardness of the initial swarf was evaluated using a micro Vickers hardness tester (SHIMADZU HMV-G31-FA-S) operating at a test load of HV0.01 (98 mN) and a dwell time of 15 s. Cross-sectional measurements were conducted by applying a 3 × 3 indentation matrix, with an indent spacing of 0.05 mm across the 0.20 mm chip thickness. Indentations were positioned at 0.025 mm from the free surface to minimize edge-relief effects. The measured hardness values resulted in an average of 98.96 HV with a standard deviation (SD) of 7.36 HV. The hardness values showed no measurable variation across the indentation matrix, indicating that the tested region of the chip exhibited a uniform hardness distribution without detectable gradients along the thickness direction.

The as-received AZ80 swarf were mechanically crushed to reduce the chip size and obtain a representative fraction suitable for X-ray diffraction (XRD) analysis on a diffractometer (RIGAKU MiniFlex600). The crushed material was examined over the range 30–60° (2θ), using a step size of 0.02° and a scan rate of 0.5°/min. The resulting diffraction pattern is presented in Fig. 3.

The diffractogram revealed the α-Mg phase as the dominant constituent, accompanied by reflections of the β-$Mg_{17}Al_{12}$ phase, partially overlapped with the main α-Mg peaks. Within the scanned angular range, no discrete reflections attributable to MgO were resolved. This absence is attributed to the low volume fraction and likely amorphous or nanocrystalline nature of the surface oxide, which falls below standard XRD detection limits. No additional crystalline phases were detected.

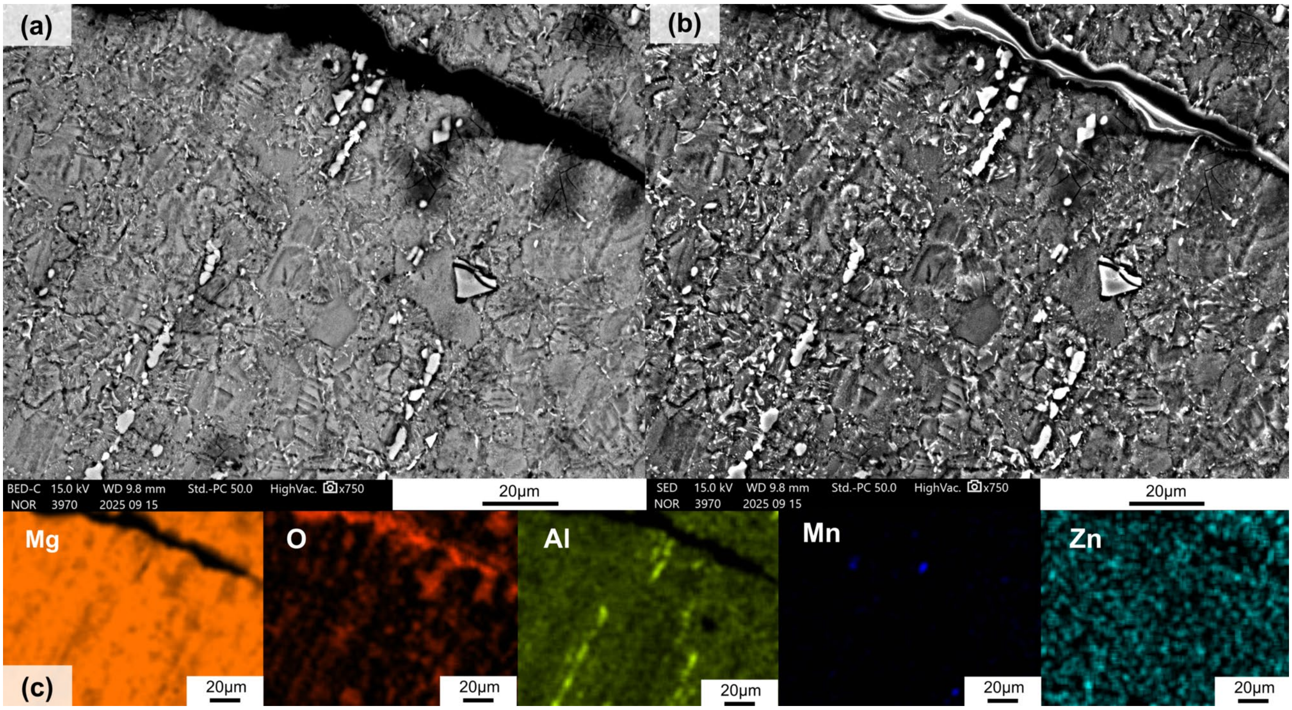

Fig. 2. (**a**) BSE and (**b**) SE images of the chip cross-section and (**c**) corresponding EDS maps.

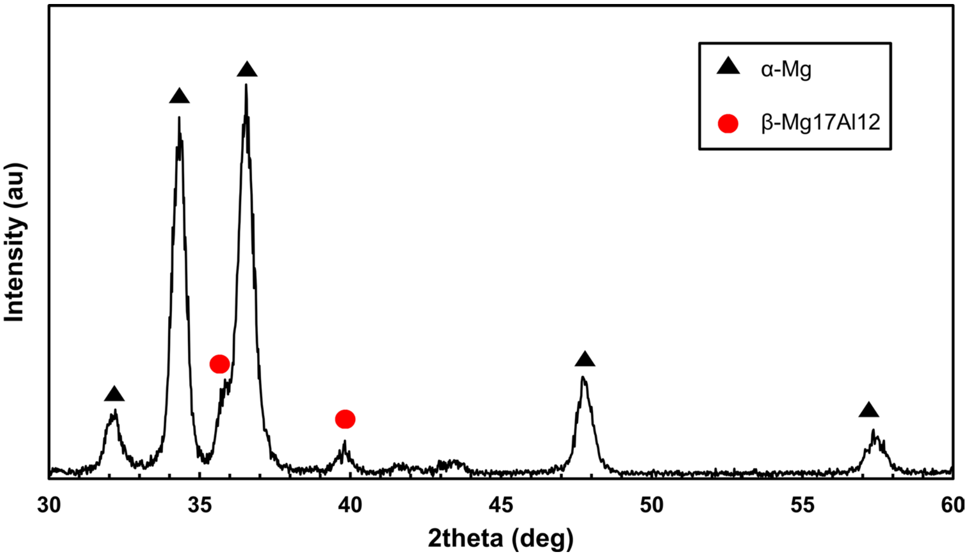

Fig. 3. XRD diffractogram of as-received AZ80-T5 chips.

Compaction setup and experimental procedure

To consolidate the as-received AZ80 swarf into briquettes suitable for subsequent processing, a uniaxial cold compaction procedure was employed. This section describes the press system, tooling configuration, initial mass preparation and the loading strategies applied during compaction.

Preparation of the swarf

The AZ80 swarf were used in the as-received condition, without pre-cleaning or thermal treatment, thereby preserving the surface oxide, chip morphology and residual machining lubricant potentially present after turning. For each experiment, 33.3 g of swarf were weighed to obtain a reproducible initial charge and briquette mass. The swarf was loosely poured into the die cavity without pre-compaction stages or vibration-assisted settling.

Compaction system and press

Compaction tests were conducted on a hydraulic servo-press (Kawasaki Hydro Engineering) with a maximum load capacity of 100 tons, operating under displacement control. The press is equipped with continuous force and ram position monitoring, allowing the direct acquisition of load–displacement curves. These data were recorded for all tests and later used to evaluate densification behavior and in-die deformation.

Tooling and assembly

The compaction tooling consisted of a solid steel housing containing a removable cylindrical sleeve (internal diameter 43 mm) which defined the briquette geometry. Two steel disks (platens) were placed at the top and bottom of the swarf bed to ensure uniform stress transfer and avoid localized indentation. The load was transmitted through a cylindrical ram extension (punch), aligned with the press axis. All tooling components in contact with the material were manufactured from H13 tool steel, quenched and tempered, and lubricated with a thin coating of boron nitride to minimize friction and prevent adhesion of Mg during compaction. The compaction tooling and the scheme of the die components are provided in Fig. 4.

To ensure the accuracy of densification measurements, the elastic deformation of the tooling under load was calculated and subsequently used to correct the displacement data, providing the actual material compaction displacement inside the die.

Compaction procedure

To investigate the mechanisms governing densification during cold briquetting of AZ80 swarf, three compaction parameters were studied: (i) the maximum pressure applied during loading, (ii) the duration of the holding time, and (iii) the pressure level maintained during the holding stage. These parameters influence chip rearrangement and the progressive collapse of internal porosity, and may also contribute to local fracture or disruption of oxide surface layers, potentially enabling closer metallic contact and thus favoring the conditions under which metallic bonding could occur. The tested conditions and corresponding nomenclature are summarized in Table 2.

Characterization of consolidated briquettes

The briquettes were sectioned along the axial plane, i.e., through the cylinder axis, using an abrasive cut-off machine fitted with a SiC wheel under continuous water cooling. This preparation exposed a longitudinal cross-section extending from the briquette center toward the external radius, which was used for all subsequent characterization.

Geometric measurements and density

The diameter was measured at four positions around each briquette and height at three positions using a digital micrometer (0.01 mm resolution). Mass was recorded with an analytical balance (± 0.01 mg). Mean values and

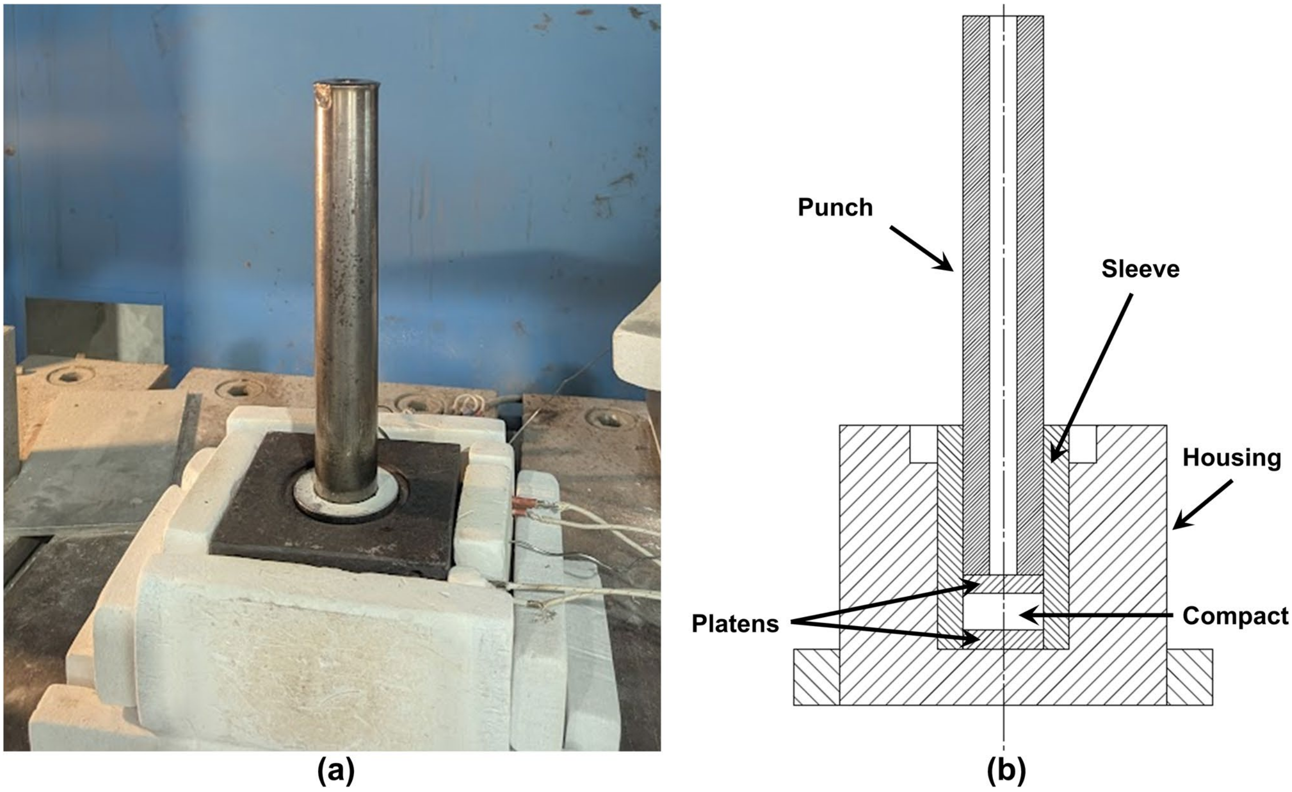

Fig. 4. Compaction tooling: (**a**) in press position and (**b**) schematic view of the components.

Test	Target load (kN)	Holding time (s)	Load during holding
T1	900	60	Passive relaxation to 450 kN
T2	750	60	Passive relaxation to 375 kN
T3	900	60	Load actively maintained
T4	900	10	Load actively maintained

Table 2. Summary of experimental tested conditions.

SDs were calculated. The as-compacted density was determined from the mass-to-volume ratio assuming a cylindrical geometry.

Porosity and inter-chip interface characterization

Polished cross-sections were imaged using a Keyence digital microscope (VHX-2000), and stitched mosaics were generated for each specimen. Image analysis was performed in MATLAB (code provided as Supplementary Information). After scale calibration, a rectangular region of interest fully inside the compacted material was selected to avoid resin and edge artefacts. Grayscale images were contrast-normalized, and pores were segmented using a hybrid approach combining global thresholding, local background correction and morphological filtering (opening, closing and hole filling). A gradient-based mask was applied to suppress polishing scratches, and an area threshold of 30 pixels^2 was used to restrict quantification to macroporosity. Limited manual verification was performed only to correct evident misclassifications.

Areal macroporosity was quantified as the fraction of pore pixels within the valid analyzed area. To evaluate the axial porosity distribution, each binary image was subdivided into five normalized horizontal bands (0 = top, 1 = bottom), and the macroporosity fraction was computed independently for each band.

SEM and EDS (JEOL IT-500) analyses were subsequently performed to characterize the inter-chip and intra-chip interfaces and to assess the nature of the contact formed under each consolidation condition.

Microhardness testing

Microhardness measurements (HV0.01, 98 mN, 15 s dwell) were performed on the axial cross-section following the same procedure and equipment described for the initial swarf in Section "AZ80-T5 Mg alloy chips characterization". Indentations were placed in a 16-point square array with 0.20 mm spacing, positioned 2 mm inward from the external surfaces. Four regions were evaluated: upper axial, lower axial, upper radial (external) and lower radial (external). This layout enabled assessing potential variations in plastic deformation across different zones of the briquette, as can be observed in Fig. 5. Mean values and SDs were calculated for each region.

Mechanical testing

From each consolidated briquette, a rectangular specimen with nominal dimensions of 10 × 10 × 15 mm was sectioned for mechanical testing. Uniaxial compression tests were carried out using a universal testing machine (Shimadzu AG-I, 50 kN) equipped with a video extensometer to measure axial strain. The tests were performed under displacement control at a constant crosshead speed corresponding to an initial strain rate of 1×10^{-3} s^{-1}. Engineering stress–strain curves were derived from the recorded load and displacement data for each specimen and used to evaluate the compressive response of the consolidated material.

Results

Consolidation behavior and green density of the briquettes

The compaction response was examined by analyzing the force–displacement evolution during loading and the force–time behavior during the holding stage. Figure 6 shows the curves obtained for the four processing conditions, allowing comparison of the densification path up to the peak load and the subsequent stress state retained during the holding period.

Figure 6a puts into evidence how specimens followed a similar densification trajectory, characterized by an initial rearrangement stage at low load followed by a progressive and exponential increase in force as the inter-chip voids were reduced. The overlap of the curves indicates a high reproducibility of the compaction response across all tests. Each briquette reached the intended peak load without instability or abrupt changes in slope.

Figure 6b presents the force–time response during the holding stage. In conditions T3 and T4, where the load was actively maintained, the force remained close to the peak value for the duration of the holding time. On the other hand, for T1 and T2, where the load was allowed to relax passively, a gradual decrease in force occurred during holding. This relaxation was accompanied by a measurable recovery of the punch position, with displacements of 1.0 mm in T1 and 0.8 mm in T2, while no displacement recovery was observed in T3 and T4.

The corresponding nominal stresses applied during compaction were calculated based on the briquette nominal diameter. Table 3 summarizes, for each condition, the peak stress and the ratio between the applied stress and the yield strength of AZ80-T5[30] at the end of compaction, and at the end of the holding period. Active load maintenance (T3 and T4) resulted in stress levels remaining close to the peak value throughout the holding, whereas passive relaxation (T1 and T2) led to reduced stress levels at the end of holding.

A representative compacted briquette, together with the final dimensions and green density values derived from mass and volume measurements, is provided in (Fig. 7).

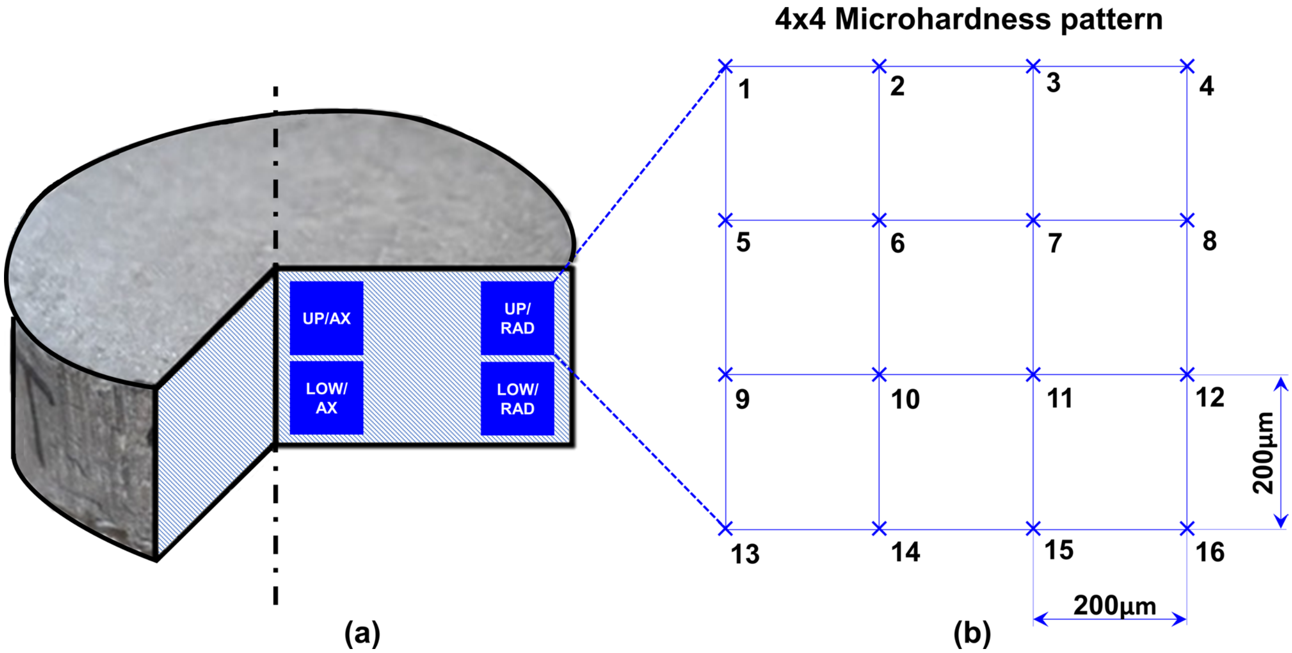

Fig. 5. Microhardness measurements: (**a**) regions analysed on the axial cross-section and (**b**) indentation pattern applied in each region.

In all conditions, the external surfaces of the briquettes appeared continuous and well-defined, without visible defects or signs of material loss (see Fig. 7a). This observation is consistent with the mass measurements recorded before and after compaction. No cracking, edge flaking, or incomplete consolidation features were observed macroscopically.

Figure 7b shows the green density obtained for the four compaction conditions. The highest density was achieved in T3 (91.7%), followed by T1 (91.4%), whereas T2 (89.2%) and especially T4 (86.9%) resulted in lower densification levels. The measured dimensions (diameter and height) for each briquette are summarized in Table 4.

The measures show low SDs across all conditions, indicating good reproducibility of the compaction process. In all cases, the final diameter was slightly larger than the nominal die diameter (43 mm), whereas the largest dimensional recovery occurred in the axial direction. To relate these macroscopic differences in green density and final geometry to the internal consolidation state, the porosity distribution and the morphology of the chip–chip interfaces were examined on polished cross-sections, as presented in Section "Macroporosity analysis".

Macroporosity analysis

The internal porosity of the compacted briquettes was assessed on longitudinal cross-sections, using the image-analysis procedure described in Section "Porosity and inter-chip interface characterization". Representative sections are shown in Fig. 8.

In T1, the compact exhibits a relatively smooth appearance with small and moderately uniform pores distributed across the section. There is no indication of connected porosity or large discontinuities, which is consistent with its green density of 91.4%. In T2, the porosity becomes more heterogeneous. The upper region shows a higher degree of consolidation, while the lower region contains larger discontinuities and several radially connected voids. This vertical gradient indicates uneven stress transmission during compaction. In T3, the macrosection displays a visible porosity level that is slightly higher than T1 but comparable to T2, with the key characteristic being its homogeneous distribution. Both the upper and lower regions show similar degrees of consolidation, and the defects remain uniform in size and spatial arrangement. There is no evidence of radially connected pores or localised defect accumulation, indicating that compaction stresses were transmitted relatively evenly throughout the compact. In T4, the porosity is more irregular and more concentrated in the lower region of the compact. Several elongated voids follow the curvature of individual chips, and wider discontinuities appear along the axial direction. This non-uniform consolidation corresponds to the lowest green density of 86.9%.

The cross-sections shown in Fig. 8 were image-processed to quantify the macroporosity within the interior region of each briquette, yielding 2.68%, 4.90%, 4.81% and 5.97% for T1, T2, T3 and T4, respectively. Cross-sections were segmented axially into five regions to quantify porosity distribution. Figure 9 illustrates the corresponding gradients, plotted from 0 (top) to 1 (bottom).

Figure 9 shows that T1 exhibits the lowest porosity and a uniform axial distribution. T2 shows higher porosity with a clear gradient increasing towards the bottom, whereas T3 displays a similar average porosity to T2 but with a smoother axial profile. T4 presents the highest macroporosity and severe accumulation in the lower segment. Absolute values are lower than green density estimates because the 2D analysis excluded the periphery and focused specifically on macrovoids (> 30 px^2).

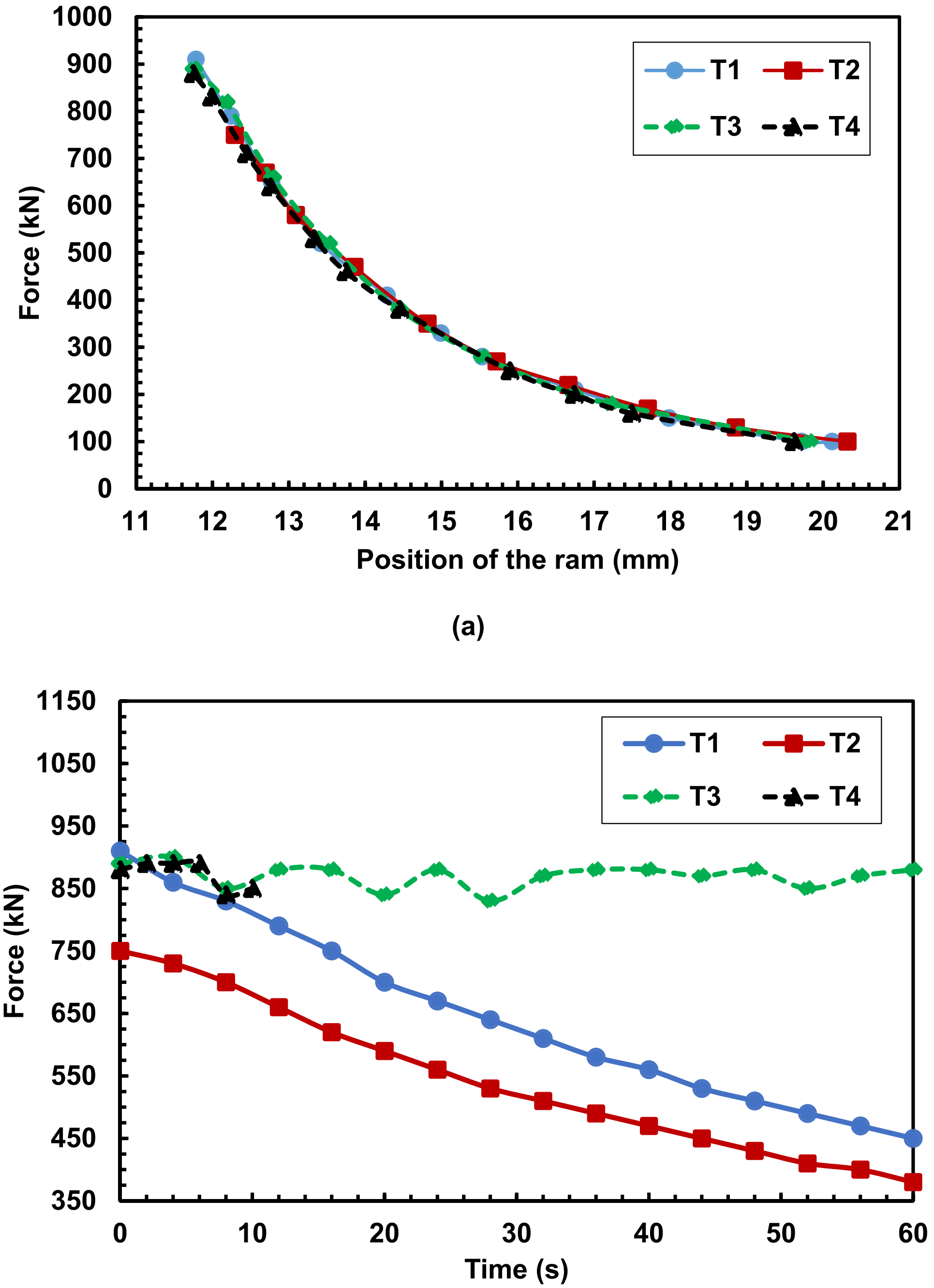

(a)

(b)

Fig. 6. (**a**) Force–ram displacement curves during compaction for conditions T1–T4, and (**b**) force–time response during the holding stage for the same conditions.

Condition	Peak stress (MPa)	σ/σy at end of compaction	σ/σy at end of holding
T1	607.8	2.20 ×	1.10 ×
T2	506.5	1.83 ×	0.91 ×
T3	607.8	2.20 ×	2.20 ×
T4	607.8	2.20 ×	2.20 ×

Table 3. Nominal stress level during compaction and holding.

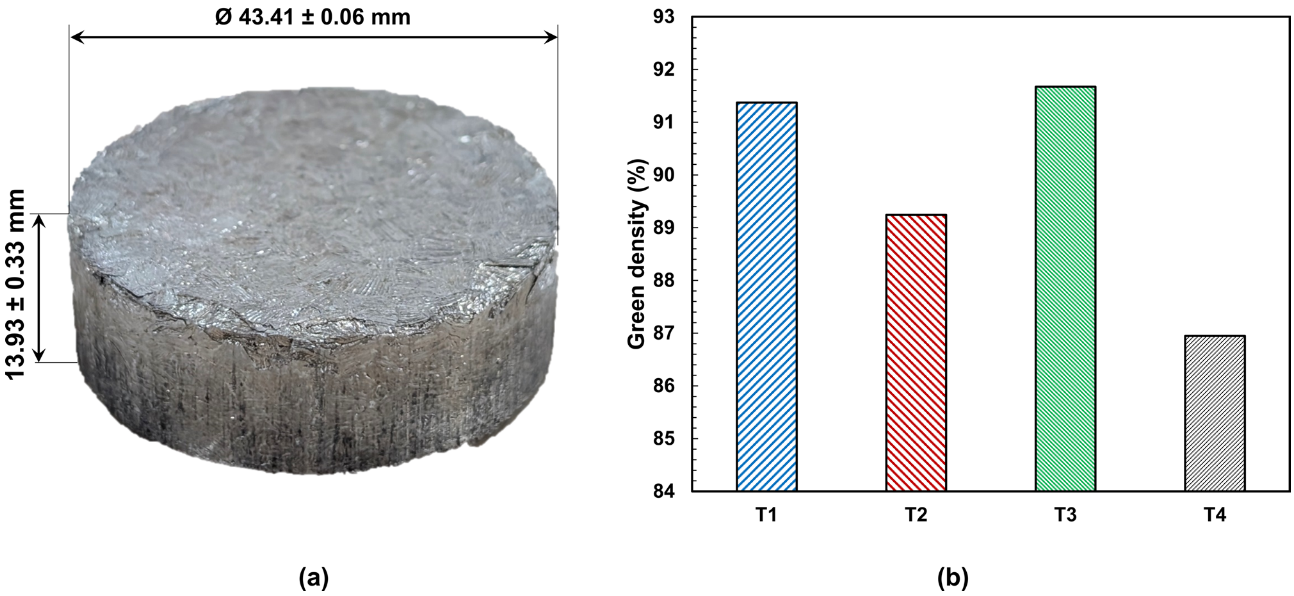

Fig. 7. (**a**) Representative compacted briquette. (**b**) Green density levels.

Condition	Diameter (mm)	SD (mm)	Height (mm)	SD (mm)
T1	43.38	0.01	13.70	0.08
T2	43.36	0.00	14.04	0.03
T3	43.40	0.01	13.64	0.06
T4	43.49	0.10	14.33	0.14

Table 4. Dimensions of the briquettes after each consolidation route.

Inter-chip and intra-chip interface analysis

To clarify the nature of the macroscopic porosity, a detailed SEM analysis was performed, including high-magnification imaging to characterize the contact quality. Figure 10 illustrates the microstructural evolution across the tested conditions, focusing on local densification and gap closure. The observations distinguish between intra-chip interfaces, corresponding to the segmentation features inherent to each chip, and inter-chip interfaces, formed between adjacent chips during compaction.

Condition T1 (Fig. 10a) presents the most consolidated appearance, where boundaries appear mostly closed and discontinuities are minimal and isolated, while T2 (Fig. 10b) shows a more heterogeneous structure with more evident localized voids. In T3 (Fig. 10c), the microstructure is characterized by consistent visual uniformity. Most inter-chip interfaces (between particles) show partial closure with reduced gap thickness, evidencing conformal physical contact between neighboring chips. Similarly, intra-chip interfaces (internal segmentation) exhibit a substantial reduction in separation, indicating that individual segments underwent effective plastic deformation to geometrically seal internal voids. In the case of T4 (Fig. 10d), it exhibits visible structural deterioration and inter-chip discontinuities are pronounced and extended, indicating that stress transmission was non-homogeneous and localized. Furthermore, intra-chip closure is irregular; while some segments are compacted, others remain separated by large interconnected voids, confirming that the processing at this stage failed to maintain the global geometric integrity achieved in previous conditions.

To further characterise these two classes of interfaces, chip-to-chip and segment-to-segment, higher-magnification SEM images were acquired in regions showing partial densification. These images were used to identify the nature of local contact, the presence of micro-voids, and potential signs of solid-state bonding.

In Fig. 11, a focused microstructural analysis was conducted on a representative region of condition T1 to characterise both inter-chip and intra-chip interfaces. The horizontal inter-chip interface appears clearly open in the BSE image and exhibits a strong and spatially extended oxygen signal in the EDS map, consistent with a non-consolidated boundary. Two inclined intra-chip interfaces were also analysed, showing different degrees of geometric closure. The first intra-chip interface (EDS line 1) presents a very narrow interfacial region in the BSE image. Although the corresponding EDS area map suggests a weak and locally discontinuous oxygen signal, the associated EDS line scan reveals a detectable oxygen maximum at the interface, confirming the persistence of an oxide layer and excluding local metal-to-metal contact. The second intra-chip interface (EDS line 2) shows a wider grey interfacial region in the BSE image and a broad and intense oxygen signal in the EDS area map. This observation is supported by the EDS line scan, which displays a single oxygen maximum at the interface. Despite the different interfacial configurations, oxygen remains detectable at all analysed interfaces, indicating

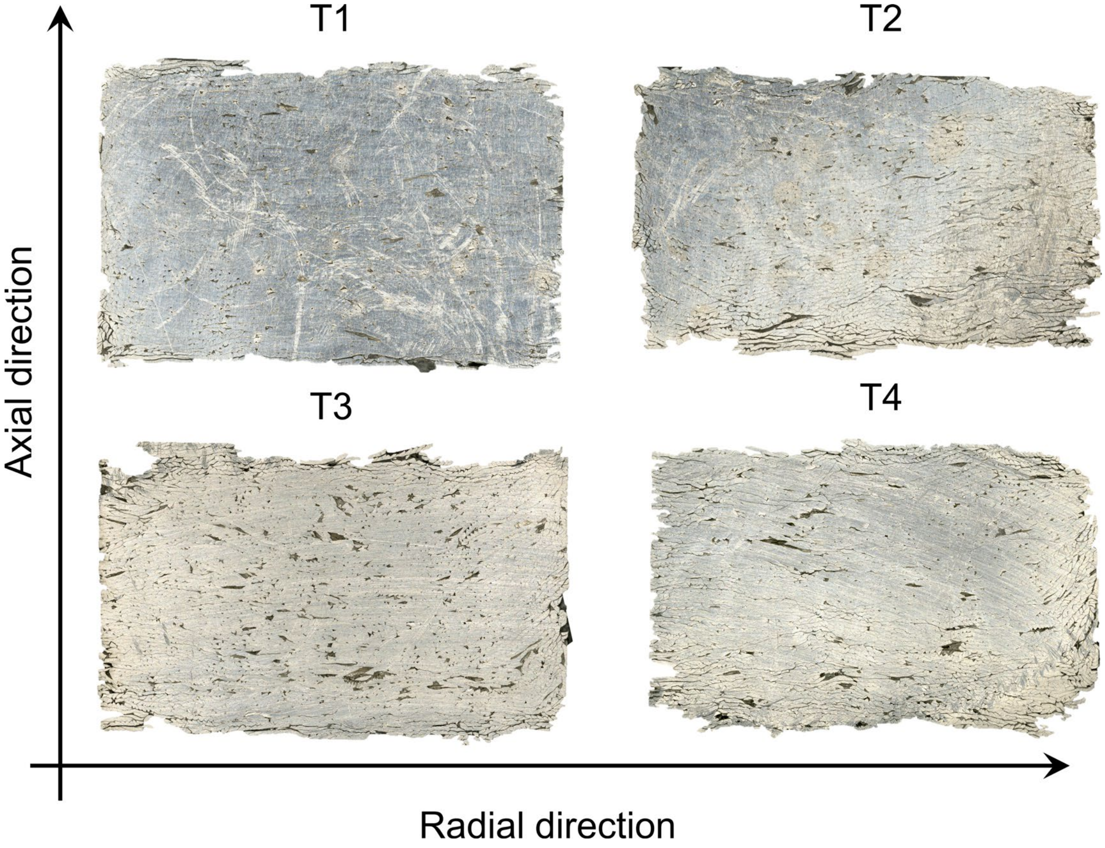

Fig. 8. Longitudinal cross-sections of briquettes compacted under conditions T1–T4.

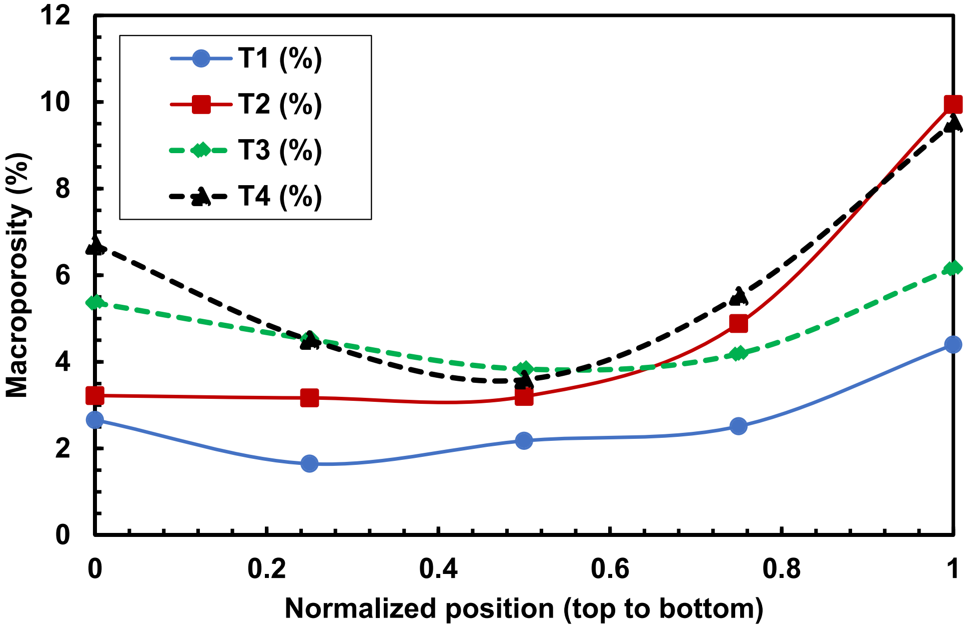

Fig. 9. Macroporosity gradient of briquettes compacted under conditions T1–T4.

that the contact character in condition T1 is predominantly oxide-to-oxide and that metallurgical bonding is not achieved. To extend the analysis beyond a single consolidation condition, highly densified regions of condition T3 were also examined at higher magnification.

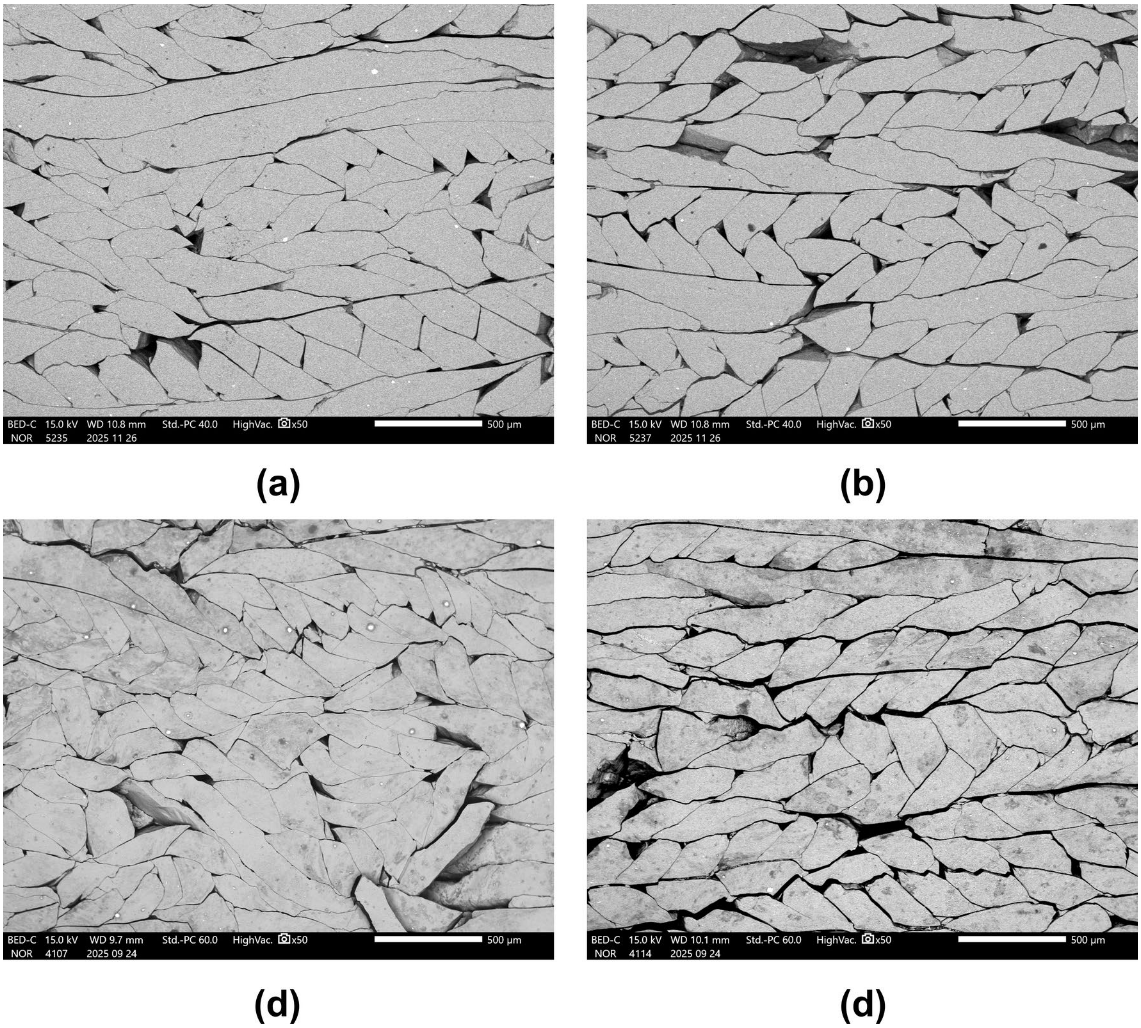

(a) **(b)**

(d) **(d)**

Fig. 10. SEM Images of compacted cross sections at × 50 magnification of (**a**) T1, (**b**) T2, (**c**) T3 and (**d**) T4.

Figure 12 provides a view of several intra-chip interfaces, illustrating the overall consolidation state achieved under conditions of high plastic deformation. These regions are characterized by pronounced geometric accommodation between opposing chip surfaces, resulting from sustained load and localized plastic flow. From this region, a locally well-consolidated intra-chip interface was selected for a more detailed analysis. At higher magnification, this interface is resolved in the BSE image as a thin grey interfacial band at the sub-micrometric scale, indicating a very tight geometric closure. The corresponding EDS map reveals a localized yet continuous oxygen signal along the interface. This observation is further supported by the associated EDS line-scan profile, which exhibits a distinct oxygen maximum centred at the interface. Therefore, these observations demonstrate that, although elevated plastic deformation promotes effective geometric sealing and close interfacial contact in condition T3, the native oxide layer remains intact and direct metal-to-metal bonding is not established.

Overall, the persistence of the oxide film across both tightly closed inter-chip interfaces and more open intra-chip regions results in a predominantly oxide-to-oxide interfacial character, with no evidence of cohesive metallurgical bonding under the investigated compaction conditions.

Microhardness

In Fig. 13, the average microhardness values of each condition are presented for a specific region of the specimen, compared to the initial value of the swarf (dash line). The vertical axis corresponds to the axial direction of the briquette, and, as described in Section "Microhardness testing", the analysis was divided into four distinct zones along this axis.

In the upper axial zone, all conditions exhibit hardness values higher than that of the initial chip material (98.96 HV). The highest hardness is recorded for condition T4 (116.06 HV), while the lowest corresponds to T3 (104.72 HV). In the upper external (radial) zone, the same trend is observed, with all conditions showing hardness values above the initial material. In this region, T4 again presents the highest hardness (111.16 HV), whereas T2 shows the lowest value (100.36 HV). When comparing the upper axial and upper radial zones, all conditions show a decrease in hardness from the axial to the external region, with the only exception being T1, which maintains a similar hardness level (approximately 100 HV).

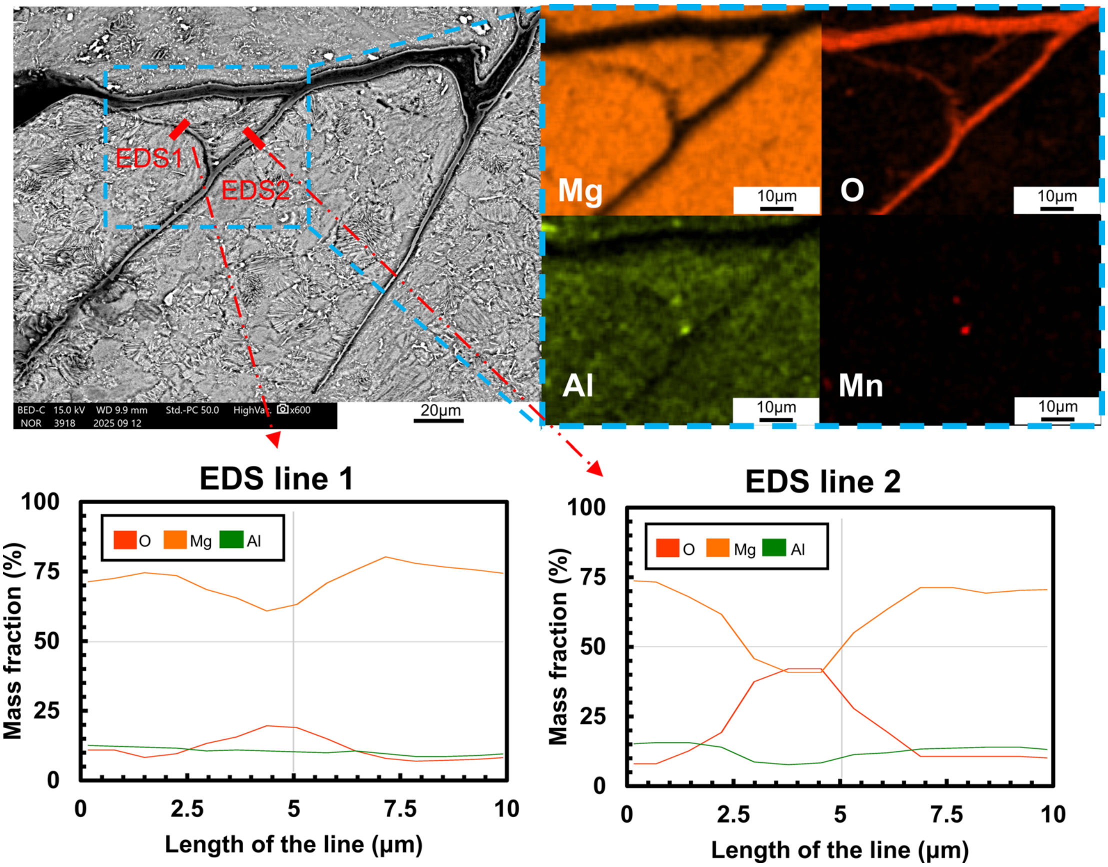

Fig. 11. SEM-BSE image and EDS analysis of T1 sample, showing inter-chip (horizontal) and intra-chip (vertical) interfaces. EDS line scans across selected intra-chip interfaces are included below.

In the lower axial zone, conditions T1, T2 and T4 display reduced hardness relative to their corresponding upper axial values, reaching 101.62 HV, 104.11 HV and 106.30 HV, respectively. These reductions represent decreases of 7.7, 3.05 and 8.4%. The only condition that deviates from this behaviour is T3, which maintains a similar average hardness in both axial zones (approximately 104 HV).

In the lower external (radial) zone, T1 and T4 exhibit the highest hardness values of all four analysed regions (114.51 HV and 116.39 HV, respectively). At this region, T3 presents the lowest hardness among all zones evaluated (97.17 HV), which is close to the value of the initial chip material. For T3, the SD is high in both the lower axial and lower external zones (31.23 and 25.02, respectively), indicating substantial variability in the local response. Condition T2 shows a hardness of 106.10 HV in this region, lower than the axial values but higher than that measured in the upper external zone.

Mechanical testing

The mechanical response of the compacted briquettes under uniaxial compression shows clear differences among consolidation conditions. Figure 14a illustrates the loading configuration and the extensometer field of view, including the gauge regions used to track axial strain. The engineering stress–strain curves are shown in Fig. 14b.

All routes show a two-stage response, where the first part of the curves is clearly non-linear: stress increases gradually, almost exponentially, as the large pores and discontinuities between and within chips begin to collapse. A dense alloy would behave differently, showing an almost linear elastic region, but instead, in the tested samples a fraction of the initial deformation is spent closing voids and creating new contact areas. The extent of this region varies. In T1 and T3 the curve becomes almost linear at strains around 0.02, whereas T2 and T4 need roughly twice that strain (~ 0.05). This agrees with their larger macroporosity and wider inter-chip gaps. After the main pores close, the curves enter an approximately linear regime (Fig. 14d). This corresponds to the response of a more continuous metallic network, with the remaining small discontinuities collapsing and the consolidated chips beginning to deform plastically. The slope differs strongly between conditions: T3 shows the highest stiffness (2964 MPa), followed by T4 (2034 MPa). T1 and T2, where pressure relaxation occurred, show much lower values (1252 and 961 MPa).

The fracture surfaces (Fig. 14c) display a plane inclined about 45 degrees to the loading axis, typical of shear-dominated failure in compression. The chip arrangement and residual porosity promote shear localisation, which explains the consistent failure mode in all cases.

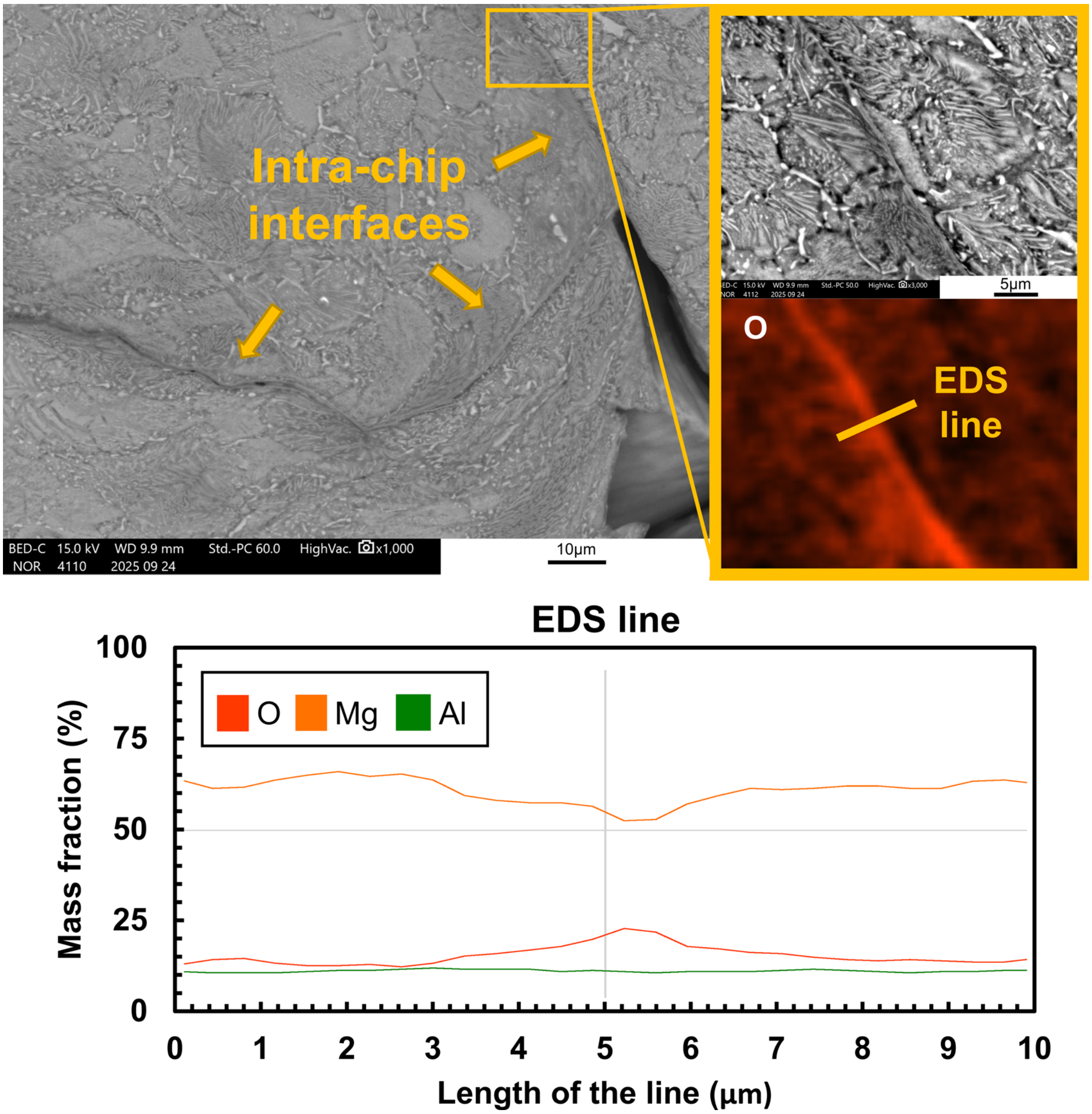

Fig. 12. SEM-BSE image of T3 intra-chip interfaces, including a high-magnification inset, oxygen map, and the corresponding EDS line scan**.**

Discussion

The consolidation behaviour of the AZ80 chip-based briquettes arises from the combined effects of chip morphology, surface condition, internal porosity distribution, lubrication residues and the time–pressure history applied during compaction. As described in Section "AZ80-T5 Mg alloy chips characterization", the chips exhibit a lamellar free surface with micro-tearing and a continuous oxide film on the tool-contact side, while the β-$Mg_{17}Al_{12}$ phase appears elongated along deformation bands. These features are characteristic of extruded Mg, and also of severe shear during machining, implying that inter-chip contact during early compaction stages occurs predominantly through oxide-covered surfaces rather than clean metal[4]. The residual traces of machining lubricant did not measurably affect chip-to-chip consolidation under the pressures and holding times explored in this study. The combination of lamellar tearing, local oxide thinning and the mechanical interlocking promoted by elongated β-phase regions facilitates partial contact development when high pressures are applied, even in the presence of thin residual films.

Green density measurements demonstrate that although high peak pressure is necessary to promote the deformation of the chips, the dominant parameter governing effective consolidation is the duration over which this pressure is maintained. T4, which records one of the highest peak pressures but the shortest holding time, attains the lowest green density, indicating that insufficient holding restricts pore collapse and prevents the establishment of stable interfacial contact. On the other hand, prolonged holding times (T3) enable the internal stresses to redistribute, promoting extensive plastic deformation in contact regions and yielding green densities comparable to T1 despite lower peak loads. Notably, allowing the pressure to decrease gradually during the holding (T1) does not compromise the final density; both T1 and T3, despite representing contrasting pressure profiles (relaxation versus sustained load), reach similar levels of compaction. These observations indicate that

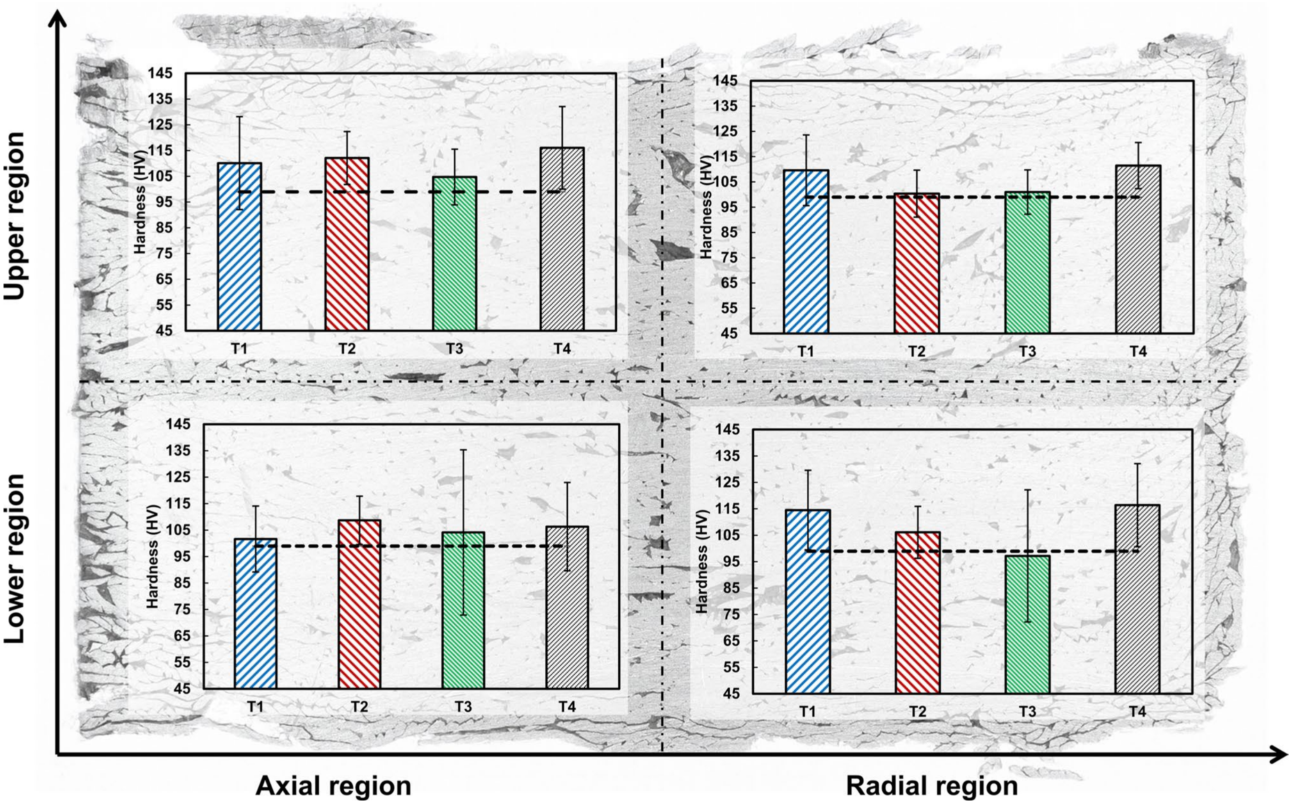

Fig. 13. Hardness maps and bar charts comparing hardness values for each condition (T1–T4) across upper/lower and axial/radial regions. The initial hardness of the swarf is indicated by a horizontal dashed line.

consolidation is governed not solely by instantaneous pressure, but by the integrated effect of pressure acting over time.

Macroporosity analysis shows that T1 develops the lowest and most uniform axial porosity distribution, consistent with the stabilising effect of controlled pressure relaxation during holding time. T2, compacted under the lowest peak pressure, exhibits a pronounced bottom-side gradient indicative of insufficient plastic flow. T3 presents porosity levels similar to or slightly lower than T2 and a much smoother axial evolution, indicating that despite its higher densification, the remaining internal heterogeneities do not develop into pronounced axial gradients.T4 displays the highest porosity and the steepest gradient, reflecting the greater sensitivity of its internal structure to the elastic height recovery that occurs upon die extraction in all conditions, which can partially reopen pores or stabilise pre-existing discontinuities. Overall, these trends highlight that managing pressure decay, as in T1, effectively mitigates recovery-induced porosity redistribution and yields a more stable internal architecture.

SEM examination provides additional insight into the influence of holding and pressure history on interfacial morphology. With short holding times (T4), the inter- and intra-chip interfaces remain more widely separated, indicating insufficient coalescence. Longer holding times (T3) promote enhanced local deformation and reduce interfacial spacing. EDS analysis show broad oxygen signals in T1, which correspond to oxidized surfaces separated by open voids, indicating a lack of close contact. The oxygen signal in T3 narrows, particularly at inter-chip boundaries. Therefore, in spite of the close physical contact achieved by high sustained pressure, the continuous oxygen-rich film persists. This confirms interface transitions from an open gap in T1 to a mechanical oxide-to-oxide contact in T3, without achieving metallic bonding. The absence of distinct MgO peaks in XRD further supports the presence of these ultrathin surface oxides, which elude bulk diffraction limits but critically dictate the interfacial behavior.

Hardness measurements reinforce these trends. In all conditions except the highly heterogeneous lower exterior region of T3, the hardness values exceed those of the original chips (98.96 HV), confirming that the severe plastic deformation imposed during compaction substantially increases dislocation density. Interestingly, T4, despite showing the lowest green density, exhibits the highest hardness in several regions, whereas the conditions with longer holding times (T1, T2 and T3) display hardness values that, while elevated, converge to a similar range. This behaviour cannot be attributed to creep, since room-temperature creep in magnesium alloys requires timescales of many hours to generate measurable strain and therefore cannot operate within the one-minute holding time[31]. The most plausible explanation is purely mechanical. During the holding stage, some regions of the chip network continue to deform plastically, while neighbouring areas that initially carried only elastic or subcritical loads undergo partial stress redistribution as the contact network settles. This coexistence of plastically active and elastically constrained domains is consistent with the intrinsically

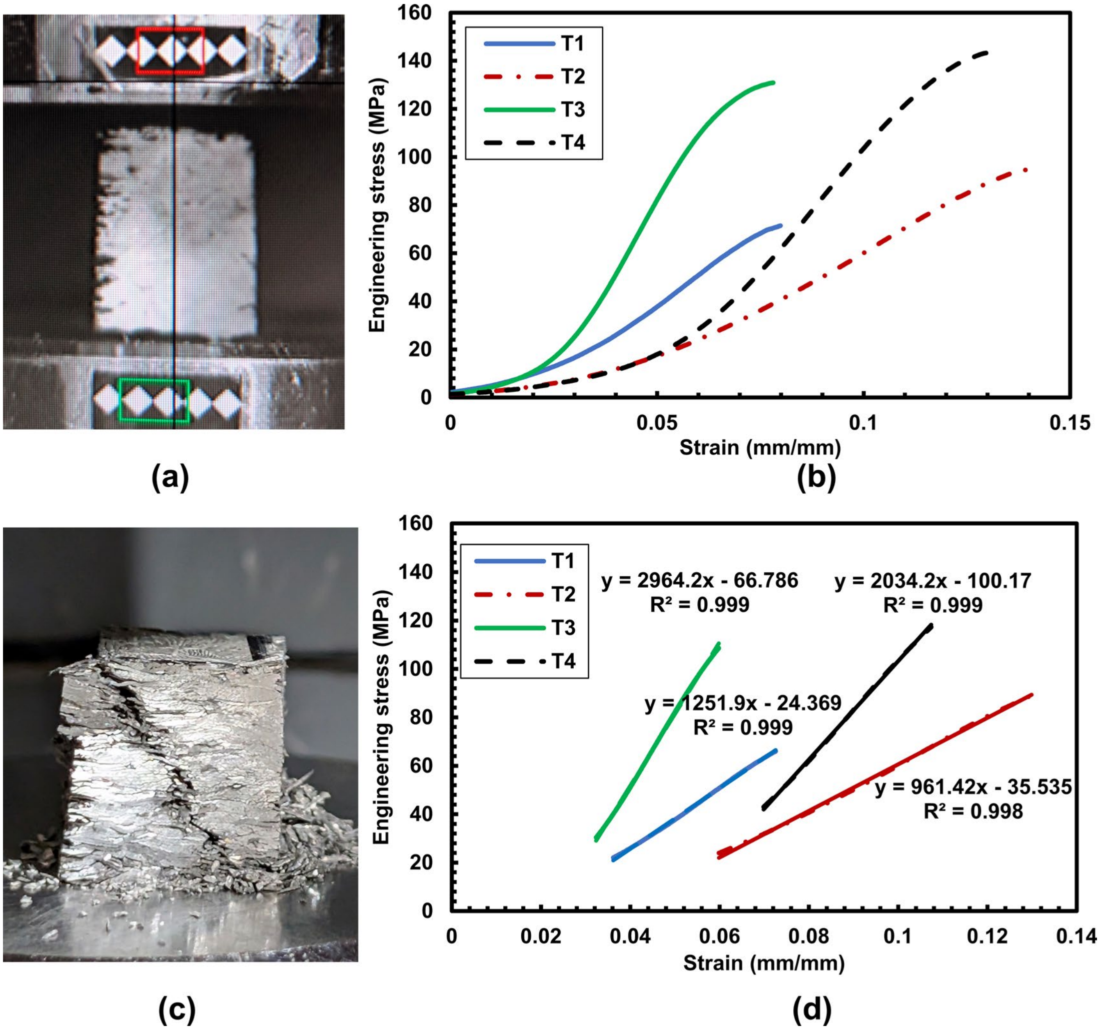

Fig. 14. (**a**) Compression test set-up. (**b**) Engineering stress–strain curves for all conditions. (**c**) Typical 45° shear fracture. (**d**) Detail of the quasi-linear region used to determine stiffness.

heterogeneous deformation behaviour of Mg alloys, where localised slip activation and partial dynamic recovery produce uneven stress partitioning under load[32]. These competing processes moderate the network hardening accumulated during the initial collapse and lead to hardness levels that stabilise within a narrower range. The large hardness dispersion in the lower region of T3 reflects this interplay, with highly work-hardened ligaments and locally relaxed or less effectively consolidated zones.

The mechanical response under compression further reflects these microstructural features. All curves exhibit an initial non-linear regime dominated by pore collapse and the progressive closure of inter- and intra-chip discontinuities. Only after these voids are eliminated does the material transition to a quasi-linear segment, corresponding to the response of a densified metallic skeleton. The strain required to reach this regime differs markedly among conditions: T1 and T3 transition around $\varepsilon \approx 0.02$, while T2 and T4 require strains closer to $\varepsilon \approx 0.05$, consistent with their higher macroporosity and larger interfacial separations. Once in the quasi-linear regime, the apparent stiffness varies substantially: T3 exhibits the highest slope (2964 MPa), followed by T4 (2034 MPa), whereas the pressure relaxation conditions yield lower values (1252 MPa for T1 and 961 MPa for T2). The fact that the more porous T3 condition exhibits higher stiffness compared to the denser T1 condition is explained by the microstructural observations. Although T1 is macroscopically denser, its interfaces retained open micro-gaps that act as discontinuities in the material skeleton. In contrast, the sustained pressure in T3 generated sub-micron inter-chip contacts and enhanced geometric closure via mechanical interlocking. This demonstrates that mechanical stiffness is governed by the quality of the interfacial contact rather than by the absolute volume of macroporosity. This effect is not fully captured by 2D image-based porosity analysis, highlighting the importance of interfacial quality and local deformation mechanisms.

All specimens fail along a plane inclined ~ 45° to the loading axis, a geometry associated with shear-dominated failure in compression[33] and consistent with the maximum shear stress criterion. The square cross-section of the samples does not alter the orientation of the critical shear plane. The presence of inter-chip interfaces and residual porosity further promotes shear localisation, favouring the formation of these inclined fracture paths and reinforcing the conclusion that the internal network, although partially consolidated, remains governed by heterogeneous stress transfer.

Conclusions

In this study, AZ80 machining chips containing residual water-based lubricants were compacted without prior cleaning, and the effects of peak pressure, holding time and pressure evolution during holding time were investigated. The findings demonstrate that consolidation is governed not only by the magnitude of the applied load, but also by the duration for which pressure is maintained and the resulting time-dependent deformation processes occurring at chip interfaces. Based on the experimental evidence obtained, the following conclusions can be drawn:

- Holding time is the main factor controlling consolidation. Longer time promotes stress redistribution and interfacial deformation, enabling green densities of ~ 91–92% (T1–T3). On the other hand, short time severely limits pore collapse and produces the lowest density (~ 87% in T4), even under peak pressures above 600 MPa.
- Axial macroporosity depends on the pressure evolution. T1 and T3 show the most uniform distributions with weak axial gradients, confirming effective pressure transmission. On the other hand, T2 and especially T4 exhibit clear bottom-side accumulation, reflecting heterogeneous stress transmission during compaction.
- Consolidation is limited by the native oxide barrier. Microstructural analysis reveals a transition from open inter-particle voids (in T1) to close oxide-to-oxide contacts (in T3). Although T3 achieves enhanced geometric closure with sub-micron interfacial spacing, the native oxide film persists across all conditions, preventing the formation of continuous metallurgical bonding. Residual lubricant traces did not measurably hinder consolidation within the explored window.
- Hardness trends reflect mechanical stress redistribution. T1 and T3, with longer times under load, show moderated hardness values (~ 100–105 HV) attributed to partial mechanical relaxation and contact network settling. T4 exhibits the highest hardness (up to ~ 110–116 HV), consistent with a state of high work hardening with minimal stress redistribution due to the short holding time.
- Stiffness is governed by interfacial quality, not just bulk density. The mechanical response transitions from pore closure to a quasi-linear regime (at $\varepsilon \approx 0.02$ in T1/T3). Condition T3 exhibited higher stiffness (2964 MPa) compared to the denser T1 (1252 MPa). This proves that the effective geometric sealing of interfaces (mechanical interlocking) is more critical for load transmission than the reduction of macroscopic porosity.

Data availability

The datasets generated during and/or analysed during the current study are available from the corresponding author on reasonable request.

Received: 1 December 2025; Accepted: 29 January 2026

References

1. Bai, J. et al. Applications of magnesium alloys for aerospace: A review. *J. Magnes. Alloys* **11**, 3609–3619 (2023).
2. Hassan, H. Z. & Saeed, N. M. Advancements and applications of lightweight structures: a comprehensive review. *Discov. Civ. Eng.* **1**, 47 (2024).
3. Hao, X., Xu, Z., Gourlay, C. M. & Li, Q. Grain refinement of magnesium castings using recycled machining chips. *Mater. Des.* **244**, 113138 (2024).
4. Paraskevas, D. et al. Solid state recycling of pure Mg and AZ31 Mg machining chips via spark plasma sintering. *Mater. Des.* **109**, 520–529 (2016).
5. Derrico, F., Farè, S. & Garces, G. The next generation of magnesium based material to sustain the intergovernmental panel on climate change policy. In *Magnesium Technology 2011* (eds Sillekens, W. H. et al.) (Springer International Publishing, 2011).
6. Shamsudin, S., Lajis, M. A. & Zhong, Z. Solid-state recycling of light metals: A review. *Adv. Mech. Eng.* https://doi.org/10.1177/1687814016661921 (2016).
7. Wan, B., Weiping, C., Lu, T., Fangfang, L. & Zhenfei, J. Review of solid state recycling of aluminum chips. *Resour. Conserv. Recycl.* **125**, 37–47 (2017).
8. Ohmann, S., Ditze, A. & Scharf, C. Semi-solid remelting of magnesium chips. *JOM* **70**, 753–757 (2018).
9. Zakaria, M. S., Mustapha, M., Azmi, A. I. & Khor, C. Y. Chip morphology and surface integrity in turning AZ31 magnesium alloy under dry machining and submerged convective cooling. *Metals* **13**, 619 (2023).
10. Shu, G., Chen, L., Dou, Z., Duan, S. & Du, J. Recycling of AZ31B alloy chips via remelting with salt flux. *Int. J. Met.* https://doi.org/10.1007/s40962-025-01558-y (2025).
11. Sabour, M. R. et al. Solid-state recycling of magnesium and its alloys via plastic deformation: An overview of processing and properties. *J. Mater. Res. Technol.* **31**, 3117–3148 (2024).
12. de Castro, M. M. et al. Consolidation of magnesium and magnesium alloy machine chips using high-pressure torsion. *Mater. Sci. Forum* **941**, 851–856 (2018).
13. Li, B., Teng, B. & Zhang, B. Integrated extrusion-shear forming process of the solid-state recycled AZ80 magnesium alloy via hot press sintering. *Acta Metall. Sin. Engl. Lett.* **33**, 351–361 (2020).
14. Ying, T., Zheng, M., Hu, X. & Wu, K. Recycling of AZ91 Mg alloy through consolidation of machined chips by extrusion and ECAP. *Trans. Nonferrous Met. Soc. China* **20**, s604–s607 (2010).
15. Consolidation of AZ31 magnesium chips using equal channel angular pressing. https://mrforum.com/product/9781644902615-24/.
16. Pei, Y., Ma, H., Yuan, M. & Teng, B. Solid state recycling of Mg–Gd–Y–Zn–Zr alloy chips by isothermal sintering and equal channel angular pressing. *J. Magnes. Alloys* **12**, 2725–2740 (2024).
17. Watanabe, H. et al. Consolidation of machined magnesium alloy chips by hot extrusion utilizing superplastic flow. *J. Mater. Sci.* **36**, 5007–5011 (2001).
18. Anilchandra, A. R., Basu, R., Samajdar, I. & Surappa, M. K. Microstructure and compression behavior of chip consolidated magnesium. *J. Mater. Res.* **27**, 709–719 (2012).

19. Zyguła, K., Lypchanskyi, O. & Skonieczna, W. Enhancing microstructural evolution and mechanical strength in recycled alsi7mg alloys through heat treatment. *JOM* **77**, 1220–1232 (2025).
20. Mabuchi, M., Kubota, K. & Higashi, K. New recycling process by extrusion for machined chips of AZ91 magnesium and mechanical properties of extruded bars. *Mater. Trans. JIM* **36**, 1249–1254 (1995).
21. Bay, N. Mechanisms producing metallic bonds in cold welding. *Weld. J.* **62**, 137–142 (1983).
22. Lapovok, R., Tomus, D. & Bettles, C. Shear deformation with imposed hydrostatic pressure for enhanced compaction of powder. *Scr. Mater.* **58**, 898–901 (2008).
23. Zhang, T., Ji, Z. & Wu, S. Effect of extrusion ratio on mechanical and corrosion properties of AZ31B alloys prepared by a solid recycling process. *Mater. Des.* **32**, 2742–2748 (2011).
24. Sharma, S. K. et al. Significance of the powder metallurgy approach and its processing parameters on the mechanical behavior of magnesium-based materials. *Nanomaterials* **15**, 92 (2025).
25. Ji, Z., Wu, S. C., Li, H. B., Hu, M. & Ming, W. Morphology of oxide and interface structure in AZ31B magnesium alloy prepared by solid state recycling. *Mater. Sci. Technol.* https://doi.org/10.1179/1743284712y.0000000134 (2013).
26. Wagiman, A. et al. Effect of thermally-treated chips on density of AlMgSi alloys recycled using solid-state technique. *Processes* **8**, 1406 (2020).
27. Chino, Y., Jae-Seol, L., Nakaura, Y., Ohori, K. & Mabuchi, M. Mechanical properties of Mg–Al–Ca alloy recycled by solid-state recycling. *Mater. Trans.* **46**, 2592–2595 (2005).
28. Wu, S., Ji, Z., Rong, S. & Hu, M. Microstructure and mechanical properties of AZ31B magnesium alloy prepared by solid-state recycling process from chips. *Trans. Nonferrous Met. Soc. China* **20**, 783–788 (2010).
29. Wang, J.-Y., Lin, Y.-N., Chang, T.-C. & Lee, S. Recycling the Magnesium Alloy AZ91D in Solid State. *Mater. Trans.* **47**, 1047–1051 (2006).
30. Zeng, G. et al. Effects of T5 Treatment on microstructure and mechanical properties at elevated temperature of AZ80-Ag alloy. *Materials* **12**, 3214 (2019).
31. Guo, T. C., Deng, Y. L., Zhang, X. M. & Zhong, Y. Y. Creep behavior of Mg–2Nd–0.5Zn–0.4Zr at ambient temperature. *Mater. Sci. Eng. A* **527**, 5801–5804 (2010).
32. Koike, J. et al. The activity of non-basal slip systems and dynamic recovery at room temperature in fine-grained AZ31B magnesium alloys. *Acta Mater.* **51**, 2055–2065 (2003).
33. Hosford, W. F. *Mechanical Behavior of Materials* (Cambridge University Press, 2005).

Acknowledgements

The authors gratefully acknowledge that this research was made possible thanks to the support of the Matsumae International Foundation (MIF). The authors would also like to thank Masayoshi Ogawa (SankyoTateyama, Inc., Sankyo Material Company) for preparing and providing the AZ80 swarf.

Author contributions

Conceptualization: Murillo-Marrodán A.; Methodology: Murillo-Marrodán A., García E., Nakata T.; Formal analysis and investigation: Murillo-Marrodán A., Nakata T.; Writing—original draft preparation: Murillo-Marrodán A.; Writing—review and editing: García E., Nakata T.; Resources: Murillo-Marrodán A., Nakata T.; Supervision: García E., Nakata T.

Funding

This work was supported by the Department of Education of the Basque Government under the Research Group program IT1507-22 and by the ELKARTEK program (Project No. KK-2025/00114). The Matsumae International Foundation (MIF) is also acknowledged for the financial support provided to this research.

Declarations

Competing interests

The authors declare no competing interests.

Additional information

Supplementary Information The online version contains supplementary material available at https://doi.org/10.1038/s41598-026-38401-1.

Correspondence and requests for materials should be addressed to A.M.-M.